Antiferromagnetic-ferromagnetic phase domain development in nanopatterned FeRh islands

R. C. Temple,[1,*] T. P. Almeida,[2] J. R. Massey,[1] K. Fallon,[2] R. Lamb,[2] S. A. Morley,[1,†] F. Maccherozzi,[3] S. S. Dhesi,[3] D. McGrouther,[2] S. McVitie,[2] T. A. Moore,[1] and C. H. Marrows[1,‡]

[1]*School of Physics and Astronomy, University of Leeds, Leeds LS2 9JT, United Kingdom*

[2]*School of Physics and Astronomy, University of Glasgow, Glasgow G12 8QQ, United Kingdom*

[3]*Diamond Light Source Ltd., Harwell Science and Innovation Campus, Didcot OX11 0DE, United Kingdom*

(Received 21 June 2018; revised manuscript received 11 September 2018; published 17 October 2018; corrected 14 November 2018)

The antiferromagnetic-to-ferromagnetic phase transition in B2-ordered FeRh is imaged in laterally confined nanopatterned islands using photoemission electron microscopy with x-ray magnetic circular dichroism contrast. The resulting magnetic images directly detail the progression in the shape and size of the FM phase domains during heating and cooling through the transition. In 5-μm-square islands this domain development during heating is shown to proceed in three distinct modes—nucleation, growth, and merging—each with subsequently greater energy costs. In 0.5-μm islands, which are smaller than the typical final domain size, the growth mode is stunted and the transition temperature is found to be reduced by 20 K. The modification to the transition temperature is found by high-resolution scanning transmission electron microscopy to be due to a 100-nm chemically disordered edge grain present as a result of ion implantation damage during the patterning. FeRh has unique possibilities for magnetic memory applications; the inevitable changes to its magnetic properties due to subtractive nanofabrication will need to be addressed in future work in order to progress from sheet films to suitable patterned devices.

DOI: 10.1103/PhysRevMaterials.2.104406

I. INTRODUCTION

The binary equiatomic ordered alloy FeRh has a magnetostructural phase transition at the unusually high temperature of approximately 370 K [1]. This is a first-order transition from an antiferromagnetic (AF) state to a ferromagnetic (FM) state and is accompanied by a 1% uniform volume expansion of the crystal lattice. The transition temperature can be manipulated by magnetic field [2], strain [3,4], chemical doping [5], and spin-polarized currents [6]. Due to this high versatility this material has been extensively investigated in recent years for its potential technological applications in heat-assisted memory recording [7], AF memory [8,9], and electric field control of magnetic order [4].

The transition specifically occurs for the B2 ordering of the crystal lattice, with the Fe atoms forming a simple cubic structure and Rh atoms at the body center position. It is mainly driven by the free energy difference between the two electronic states of G-order AF on the Fe sites and an FM state with the Fe moments aligned with a 1-μ_B moment that appears on the Rh site. Due to the first-order nature of the transition, domains of both the AF and the FM phases can coexist in the same sample [1]. Previous studies have imaged [10–13] and manipulated [14] these coexisting states and nucleation and growth of FM regions in an AF matrix have been observed.

Future applications based on novel magnetic memory will require thin-film material patterned on the nanoscale using known fabrication techniques. The properties of the FeRh phase transition are well known for bulk forms of FeRh but are modified with some variability when produced in a sheet film. FeRh films have been extensively studied and it is known that both strain and reduced symmetry at the interfaces combine to modify the transition temperature and broaden the transition width to various degrees throughout the depth of the film [15–18]. These modifications are dependent on the film thickness, crystalline order, and capping material.

Further changes to the transition arise when it is confined to lower dimensions through patterning, particularly due to phase domain shape and formation. Electronic transport in FeRh nanowires has been seen to show large supercooling effects and a highly asymmetric transition between heating and cooling [19]. There have been few studies as yet on the effects of lateral confinement of the FeRh layer [20].

In this investigation we use x-ray photoemission microscopy (XPEEM) to obtain magnetically sensitive images of a patterned FeRh film. The lateral confinement is in square islands of side lengths 0.5, 1, and 5 μm, below and above the final typical FM domain size of ∼1 μm [10–13]. Following a description of the fabrication and characterization of our samples in Sec. II, our results are presented in two main sections. In Sec. III A we examine phase domain development in a 5-μm island and show the three stages of domain creation and propagation. In Sec. III B we compare this transition domain behavior to that of the more confined 1- and 0.5-μm islands and discuss the consequences of the changes observed in the context of future technological development. We give our conclusion in Sec. IV.

*r.c.temple@leeds.ac.uk

†Present address: Physics Department, University of California, Santa Cruz, Santa Cruz, California 95064, USA.

‡c.h.marrows@leeds.ac.uk

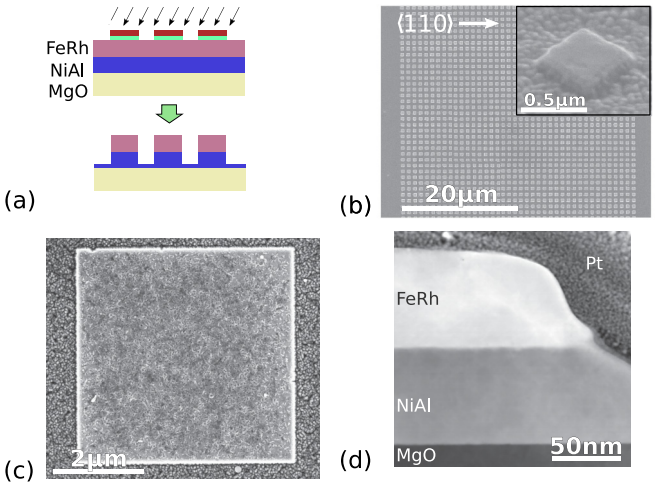

FIG. 1. FeRh nanopatterned islands. (a) Diagram of the nanofabrication process; see the text for a full explanation. (b) SEM image of the array of 0.5-μm squares. Inset: Closeup image of one of the islands taken at a 45° angle to the film plane. The damage to the NiAl layer from the ion milling is shown. (c) In-lens detection SEM image of a 5-μm island highlighting the grain edges. (d) Cross-section TEM on the edge of a 5-μm island using annular dark-field contrast.

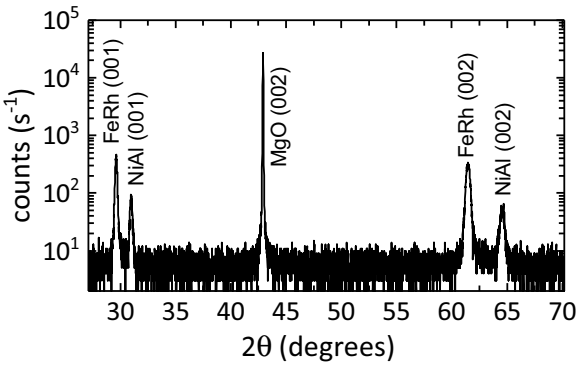

FIG. 2. X-ray diffraction of the NiAl/FeRh sheet film in the Bragg-Brentano geometry showing the B2 crystal structure.

II. MATERIAL CHARACTERIZATION

The patterned film that we studied is a NiAl (70 nm)/FeRh (70 nm) bilayer deposited on an MgO (001)-oriented substrate using dc magnetron sputtering at 600°C. This was followed by a 60-min anneal at 700°C in a vacuum pressure of 1×10^{-5} Pa in order to form the required B2 crystal structure. Further details of the FeRh deposition are given elsewhere [21]. Standard e-beam lithography using a JEOL JBX-6300FS system followed by e-beam evaporation was used in a positive liftoff process to create an Al/Ti hard mask of square islands with side lengths of 0.5, 1, and 5 μm, all separated on a grid structure with one-island-width gaps (the spacing was designed to negate magnetic dipolar interactions between the islands). The mask was transferred to the sheet film by Ar^+ ion milling from a 1-kV source at a 30° incidence angle under continuous rotation to a target thickness of 20 nm NiAl. The NiAl is a paramagnetic metal with a B2 structure lattice matched to the FeRh and is required as a path to ground for the photoemission current during the XPEEM experiment. Finally, the metal mask was removed with a standard Al chemical etch to reveal the bare FeRh surface. A diagram of this process is shown in Fig. 1(a). All of the islands shown in this paper were created with straight edges along the ⟨110⟩ crystal orientations of the FeRh. XPEEM is a surface sensitive technique so the chemical etch was employed, as it was necessary to protect the FeRh surface from the ion milling. FeRh is resilient to chemical degradation and oxidation due to the high Rh content [22].

Figure 1(b) shows a scanning electron microscope (SEM) secondary electron emission image of a final patterned array of NiAl/FeRh islands of side 0.5 μm. The inset shows, at a 45° angle to the film surface, the rough surface of the surrounding NiAl. This is thought to be due to preferential milling at grain boundaries enhancing any roughness present in the as-deposited film. This is also shown in Fig. 1(c), an SEM image of a 5-μm island using an in-lens detector to highlight gradients in the topography.

Scanning transmission electron microscopy (STEM) was utilized to image a cross section of the sample taken through a 5-μm island after the XPEEM imaging experiment. The sectioned specimen was created using a focused ion beam "liftout" technique [13] and produced with an estimated thickness of between 50 and 120 nm. Figure 1(d) shows a high-angle annular dark-field (HAADF) image, sensitive to atomic number contrast, obtained from one of the edges of the island. The MgO, NiAl, and FeRh layers are easily distinguished, as are the protective electron and ion beam deposited Pt layers from the cross-sectioning process (the Pt is deposited after the magnetic XPEEM measurements). The fabricated island is observed to have a sloping edge with an average angle of 30° relative to the vertical.

The epitaxy of the material was confirmed with x-ray diffraction shown in Fig. 2. The B2 (CsCl) phase of the FeRh is identified with the clear (001) superstructure peak; no other phases are detected. The ratio of the (001)-to-(002) peak intensities gives a chemical order parameter of 0.8 (where 1 is fully B2 ordered and 0 is in the random bcc state [23]). The NiAl is also in the B2 phase with a lattice parameter of 2.884 Å. The bulk lattice parameter of FeRh is 2.99 Å [15] so that the NiAl introduces lattice mismatch strain of −5.3% on the FeRh film. The FeRh lattice parameters of the free film were determined to be $a = 2.972$ Å and $c = 3.013$ Å, showing the expected tetragonal distortion.

The XPEEM imaging was done on beamline I06 at Diamond Light Source in the XPEEM end station on and off the Fe L_3 resonance. The probing depth of the technique is approximately 3 nm. Electron yield intensity images were recorded using positive circular polarized I^+ and negative circular polarized radiation I^- on (at energy 706.6 eV) and off (700 eV) the Fe L_3 absorption edge. On the L_3 edge there will be x-ray magnetic circular dichroism (XMCD) contrast that yields information about FM ordered regions. The four sets of images of each polarization on and off the resonance edge were averaged and then normalized to a defocused image and the off-resonance images were subtracted to obtain the difference signal $d^{\pm} = I^{\pm}_{\text{on}} - I^{\pm}_{\text{off}}$. The final quantity displayed in the XMCD images is given as $D = (d^+ - d^-)/(d^+ + d^-)$.

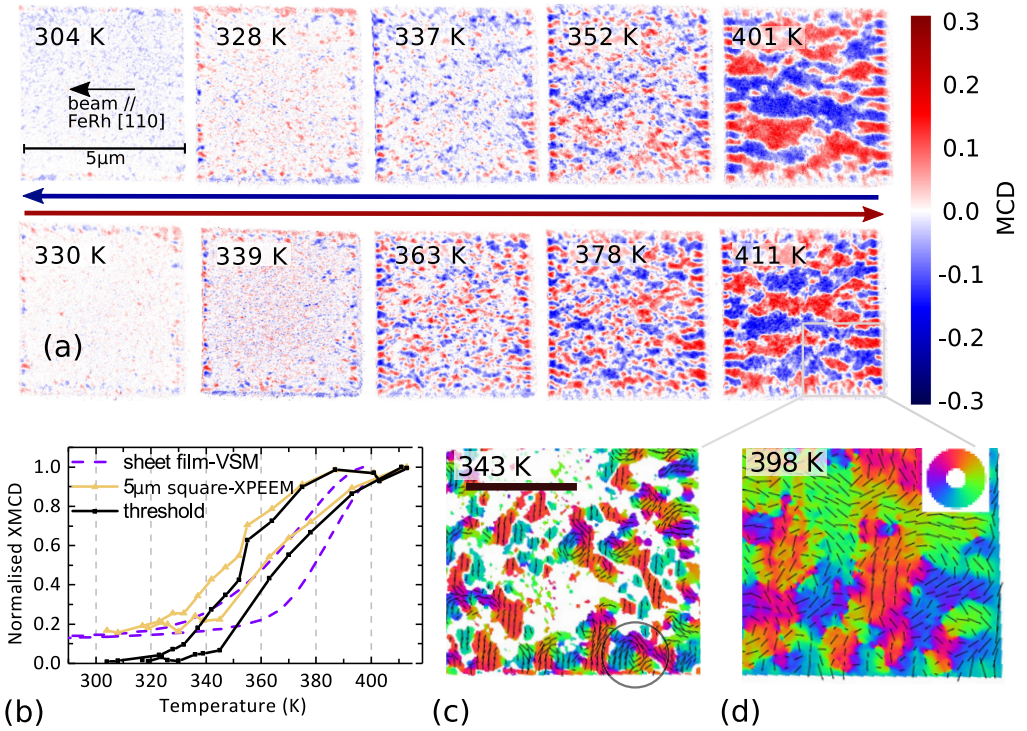

FIG. 3. XPEEM imaging of FM domains. (a) Magnetic dichroism images of an island of side 5 μm shown as a function of the temperature during the cooling process (upper row of images) and the heating process (lower row). The beam direction and magnetic sensitivity are shown in the top left image. (b) Integrated absolute XMCD signal as a function of the temperature and in comparison to a VSM measurement. Both signals are normalized to the saturation value. The threshold signal is also shown; see text for details. (c), (d) Vector magnetization maps of the bottom right portion of the 5-μm island during heating. The scale bar in (c) is 1 μm. The color represents the vector direction indicated in the color wheel and the length of an arrow represents the local XMCD magnitude. A vortex state is highlighted in (c).

III. RESULTS

A. Magnetic and phase domain behavior

In Fig. 3(a) the dichroism images from a 5-μm island are shown at a series of temperatures on the heating and cooling branch of the transition. The color map shows red and blue domains that are ferromagnetic, with magnetizations having components parallel and antiparallel to the incoming beam direction. White areas have no XMCD signal and are either antiferromagnetic or magnetized perpendicular to the beam direction. As the temperature increases the ferromagnetic regions grow until the entire square has reached the ferromagnetic phase and has a central magnetic domain width on the scale of 1 μm. As has been previously observed in sheet film samples [10], the reverse transition occurs in a qualitatively similar manner. The temperatures for the heating and cooling branches are chosen at values of similar absolute magnetization and are therefore offset due to hysteresis in the transition as observed below.

The summed absolute XMCD signals for images at each temperature are plotted in orange in Fig. 3(b) and compared to SQUID vibrating sample magnetometry (VSM) measurements of the complete film before patterning. Both signals are normalized relative to their maximum value and plotted on the same scale. The VSM measurements were done under an in-plane (parallel to the ⟨110⟩ direction) saturating field of 0.1 T, while the XPEEM measurements are necessarily done in a remanent state. An approximately 10 K hysteresis is seen in the transition upon heating and cooling for each measurement. This is a well-documented effect in the AF-FM FeRh and other first-order transition systems where phases can coexist in the same volume [1]. While the general shape of the loop is the same in both measurements there is a clear 20 K offset between the VSM and the XPEEM data. This is thought to be due to the difference between the VSM technique, which detects the average magnetization throughout the sheet film, and the XPEEM, which looks only at the surface state in a small region of the film. Thin-film FeRh has been shown to have a lower transition temperature by up to 70 K at the top surface, particularly in capped samples, but this has been observed even when uncapped [16,24,25]. This is generally attributed to strain relaxation and symmetry breaking at the interface. We cannot rule out some contribution of the change in transition temperature resulting from uncertainties in the thermometry from the two techniques also.

The nonzero magnetization in the AF state seen in the VSM data is a common effect in FeRh and studies have shown that this is due to a small strain stabilized ferromagnetic region close to the bottom interface of the film most easily observed with a technique like polarized neutron reflectometry [16,17,25]. We are not able to image the magnetic domains at the NiAl/FeRh interface due to the small probing depth of the XPEEM technique (polarized neutron reflectometry is not possible on such small islands). The nonzero signal we see in the XPEEM data at low temperatures is caused by residual noise in regions of the island with zero

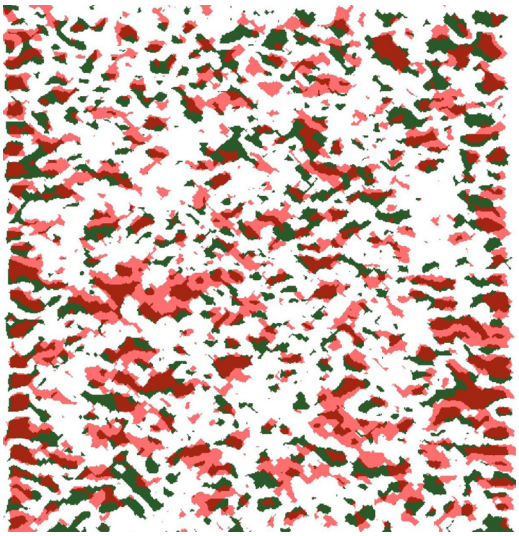

FIG. 4. The 363 K XMCD image from the heating arm (green) and 352 K XMCD image from the cooling arm (light red) made binary using a threshold value and overlaid for comparison (overlap, dark red). The full 5-μm island is shown. A high percentage of the domain sites is shown to overlap.

magnetization; this does not average to 0 since we take the integral over the absolute XMCD signal D. The small threshold of $|D| > 0.03$ is applied to the signal to eliminate this noise prior to the integral (the root mean square amplitude of the noise is 0.01). Using this threshold produces the black curve shown in Fig. 3(b). Within the experimental limitation no magnetic signal is detected in the AF state at the top surface.

The magnetic domains are examined in Figs. 3(c) and 3(d). These are vector maps, obtained by combining dichroism images at two perpendicular rotations of the sample with respect to the x-ray beam. At the midtransition point these domains form flux closure structures, with a vortex state particularly visible in Fig. 3(c). In the fully ferromagnetic state the flux closure still exists but much larger domains are present.

While the dichroism images contain information on the direction of the magnetization, it is important to distinguish between standard magnetic domains—ubiquitous in ferromagnetic materials—and *phase* domains, which are contiguous volumes that have undergone transition to the FM state regardless of their magnetic direction. These phase domains can be best seen using the absolute dichroism signal $|D|$, which makes no distinction between parallel and antiparallel magnetisations.

From the images in Fig. 3(a) we see that the phase domain creation proceeds by a nucleation and growth mechanism. Looking in more detail at the heating and cooling arms many of the local area transition temperatures are seen to be similar in both arms for comparable states. In Fig. 4 the image at 363 K on the cooling arm has been overlaid on the image at 352 K on the heating arm. These are both shown as binary images so that all ferromagnetic domains appear one color and areas with no magnetic signal are white. Forty-four percent of the FM pixels in the heating arm overlap with the cooling arm, as opposed to an expected 26% for a random distribution of the pixels in the image. This result is similar for both domains at the edge of the island and domains in the the central region.

FeRh undergoes volume expansion during the AF-to-FM phase transition; this could be expected to create a local dynamic strain landscape around areas that have undergone transition. Tensile strain is known to lower the transition temperature [3]. It is clear from the similar domain positions in the overlaid images, however, that there is a static background energy landscape that plays the dominant role in the energetics of the transition, at least on the >100-nm length and measurement time scale of approximately 30 s.

One of the complications in applying simple first-order models to FeRh is that the volume expansion of the lattice as it undergoes transition will create a dynamical strain landscape over the material as phase domains alter. This local strain may affect the development of local domains, allowing them to grow at lower temperatures than they would be able to otherwise. Tensile strain is known to lower the transition temperature [3]. In this data we see no obvious preference for nucleation of domains close to other current nucleated sites. It is clear from the similar domain positions in the overlaid images, however, that there is a static background energy landscape that plays a larger role in the transition than the dynamic landscape, at least on the >100-nm length and measurement time scale of approximately 30 s.

We can further examine the phase domain formation using the binary images to find the sizes of the phase domains. In Fig. 5(a) an area-weighted histogram of the domain equivalent diameter d_{eq} is plotted for various temperatures on the heating arm. The domain characteristic size d_{eq} is calculated simply from the total domain area as $d_{eq} = 2\sqrt{A/\pi}$. The histogram count has been weighted by the domain area A in order to balance the space preference for large compared to small domains.

From 345 to 378 K the weighted histograms are simple peaked distributions. As the temperature increases the total number of domains increases, as does the peak center size and the peak width. The histogram peaks have all been fitted with Gaussian distributions, which are shown in the histogram, and the peak centers and widths are plotted in Fig. 5(b). While the peak trend is clear, the noise observed in the individual counts is due to normal statistical fluctuations in the small sample of domains within the island area. The domain sample is small due to the naturally occurring domain size relative to the patterned island size.

Importantly, this demonstrates that both nucleation and growth are taking place simultaneously at these lower temperatures. Domains nucleate at a typical size of <200 nm in locations determined by the static background energy landscape and at a size that is a balance between the competing strain and electronic thermodynamic cost of nucleation and the magnetostatic cost of not forming a flux closed domain. From the histogram we see that the majority of the domains are newly nucleated below 363 K. From 363 to 378 K the majority of the phase domain area increase proceeds by domain growth as opposed to nucleation, as can be clearly seen in the dichroism images. At 393 K there remains a broad low-diameter peak but a new region of the distribution opens up at larger diameters, greater than 1 μm. This is the final stage of phase growth, where percolation has been reached and domains coalesce

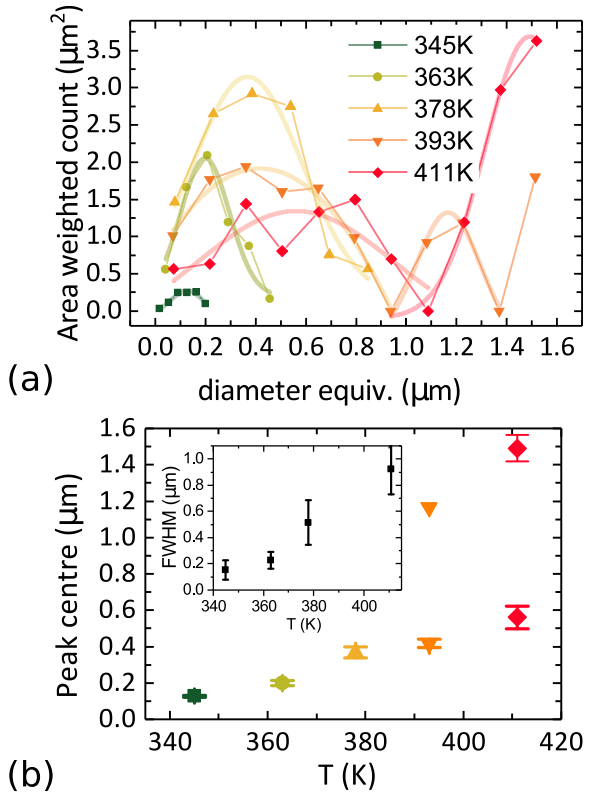

FIG. 5. Characteristic sizes of FM domains. (a) Area-weighted histogram of the domain size at various temperatures during the heating process. See text for details. (b) Peak centers of Gaussian peak fits to the histograms in (a). Inset: Peak full width half-maxima (FWHM) are plotted.

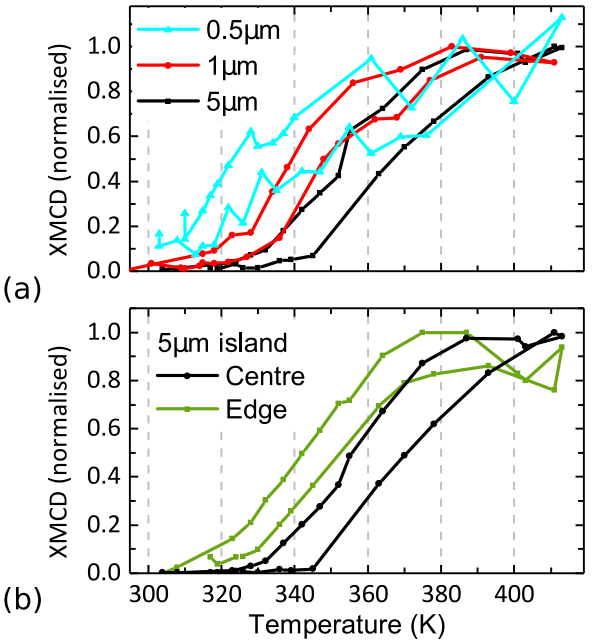

FIG. 6. Phase transition measured by XMCD. (a) Absolute dichroism integrated over the entire island for 0.5-, 1-, and 5-μm island sizes shown on the same scale. For the smaller two sizes an average signal over four FeRh islands has been plotted. (b) Integrated dichroism signal vs temperature for the 5-μm island. The integral is over the edge and central area of the island as indicated.

with neighboring domains. Finally, at 411 K the majority of the central domains are merged and form a peak in this larger-diameter region. The edge domains remain somewhat separated and smaller than the central domain.

These histograms make the boundary between the three growth modes, nucleation, growth, and merging, very clear in a way not observed before. It is only when there is little growth available left to the FM domains that they will merge. There is clearly an energy cost in the magnetostatic energy of the domain formation. It may be due to the topological stability of the vortex cores in the smaller domains.

It is noted that the final magnetic domains have an elongated shape approximately three times longer along the beam direction in this case. This nematic ordering has been seen before in XPEEM experiments on Pd-doped FeRh and was attributed to a martensitic transition [11]. In this case without the Pd doping, that cannot be the case. FeRh has a very weak (cubic) anisotropy [26] and small stray magnetic fields can generate a stripe domain magnetostatic locking pattern [27]. This could potentially be the reason for the nematic ordering, however, further investigations under a controlled magnetic field are necessary.

B. Size effects

The integrated signal plot for the 0.5-, 1-, and 5-μm island sizes is shown in Fig. 6(a). As discussed before, asymmetry levels below 0.03 have not been included in the integration and the signals have been normalized to their saturation value. The transition temperature is shown to be reduced in the smaller islands. The transition temperature is calculated at the midpoint of the transition, where 50% of the magnetic signal remains. On the cooling arm it is found that the 1-μm size has a transition temperature of 343 K, 12 K cooler than that of the 5-μm island, and the 0.5-μm island size one of ≈333 K, a further 10 K below that. The smaller islands show significantly more noise in the integrated signal, making exact quantification of this offset difficult. This noise is a systematic issue caused by the sensitivity of the images to the background subtraction and drift correction process. Any errors in this process have a consequently larger effect on smaller regions of the image.

It is clear from the images of the 5-μm island in Fig. 3(a) that the transition temperature is reduced at the edge of the island. Phase domain nucleation occurs at a lower temperature on the edges of the patterned island and these domains grow while the central domains are still nucleating. The hysteresis loops of the edge and central region are compared directly in Fig. 6(b) (again, fluctuations observed here are due to errors in the background subtraction). At 339 K during the heating process the majority of the island within 300 nm of the edge has nucleated ferromagnetic states, while the middle of the square has approximately nine nucleated domains, comprising approximately 0.01% of the central island area. In Fig. 7(a) we show a color-coded map of the transition temperature over the image area. For this image and other transition maps in the figure a 6-pixel moving average smoothing has been

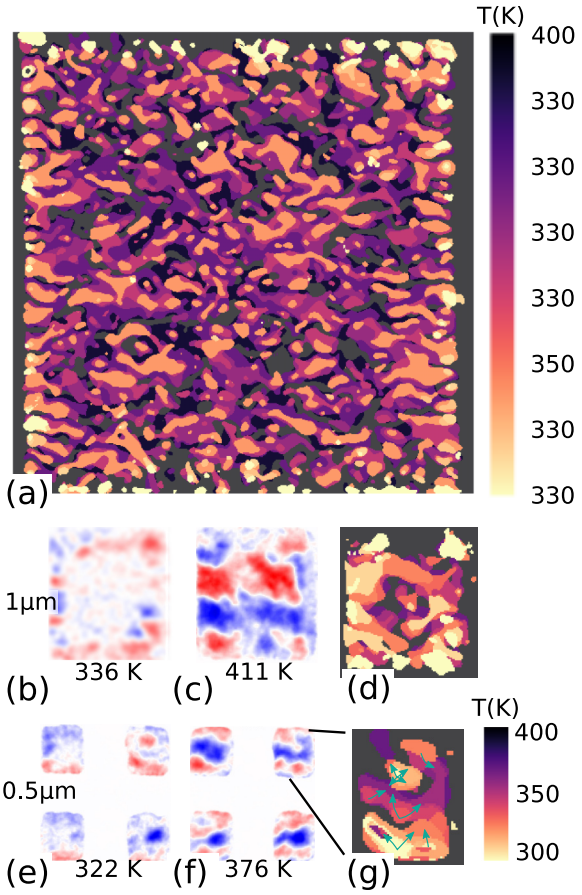

FIG. 7. Size dependence of the phase transition temperature. (a) Map of the phase transition temperature for a 5-μm island. The absolute signal is used so only phase domains are shown. (b), (c) Dichroism images from a 1-μm island using the same color scheme as in Fig. 3 at the respective indicated temperatures. (d) Temperature map of the transition using the same color scale as for (a). (e), (f) Dichroism images for the 500-nm island size including four separated islands with edge effects less evident. (g) Temperature map of the highlighted island in (f), with a slightly altered color scale. Domain nucleation sites are isolated bright regions; domain propagation directions from the nucleation sites are indicated by arrows.

applied to the raw data, and the threshold for transition is set at an asymmetry of $|D| > 0.015$. The edge nucleations are highlighted by the brighter colors around the edge and nucleated areas are seen to grow inwards towards the center of the island as the temperature increases.

These edge effects are expected to play a more important role for smaller islands, and indeed this is what we find. Figures 7(b) and 7(c) show dichroism images of a 1-μm island during nucleation at 336 K and posttransition at 411 K, respectively. We see in Fig. 7(b) the same edge-state nucleation pattern. In this case the edge width is 200 nm. Again, this is highlighted in the transition map shown in Fig. 7(d), where the growth inwards of the edge nucleations is clearly shown.

For 0.5-μm islands, which were the smallest we could obtain a clear dichroism signal from, a separate edge nucleation process is not evident. There are fewer nucleation events so the statistics are poor but these are not seen to be biased towards the edge regions of the island. Images including four such adjacent islands are shown in Figs. 7(e) and 7(f) during the nucleation phase and posttransition. A transition temperature map of the upper right island is shown in Fig. 7(g). In the map we see that just six nucleation events trigger the phase domain growth over the island; propagation vectors for this growth are shown. This is perhaps not unexpected, since the edge domains on the larger islands were >200 nm. For a 500-nm island nearly the entire surface will be within the effective edge region.

The initial edge nucleation in the 5- and 1-μm islands occur at similar temperatures of 330 K. The offset in the average transition temperature is simply due to the relative proportion of the island in the edge nucleation region: $(19 \pm 1)\%$ and $(64 \pm 1)\%$ of the total island area, respectively, for the two sizes. The initial nucleation of the 0.5-μm island is at approximately 310 K, lower than for the larger islands. The offset in the phase transition temperature at the higher temperatures is due to the rapid progress of the transition once nucleated. Fewer nucleation events mean that fewer phase domain merging energy barriers have to be overcome, as with the edge of larger islands the FM domains rapidly grow to fill the space.

The question which remains is, What is the mechanism by which the edge properties are modified? There are two likely potential causes. Subtractive patterning of the sheet FeRh film, forming edges (of the islands), enables the release of strain caused by mismatch of the natural FeRh lattice parameter with the MgO substrate lattice parameter; this strain relief is greatest in smaller islands. In work on Si pillars this has been found to relieve up to 50% of the strain in 500-nm pillars [28]. This alone would certainly generate a large change in the transition parameter; a change of 30 K has been measured previously for thick FeRh films under differing strain conditions [15]. However, the strain relief would be far lower than this in the larger, 5-μm island, yet we see that the edge domains are of a similar size and the change in transition temperature is similar to that of the much smaller islands. Natural edge roughness visible in the SEM images [Fig. 1(b)] could contribute to the relief.

A second possible cause is collision damage from the Ar^+ ion milling process. Ion milling damage during the mask transfer is a well-documented phenomenon in magnetic medium patterning [29] and other fields. Due to the titanium mask all damage to the FeRh island will be at the sidewalls. FeRh is known to be particularly sensitive to ion damage [30] and its signature has been observed in TEM cross-sectional samples of FeRh prepared by 2-keV Ar^+ ion milling [31]. Controlled ion beam damage experiments have shown that low doses will initially lower the transition temperature by several tens of kelvins, followed by complete removal of the transition at higher doses, leaving a purely ferromagnetic material [30]. Using TRIM simulation software [32] for 1-keV Ar^+ ions impinging on FeRh we find a penetration depth of up to 5 nm. However, this does not take into account ion-channeling effects in crystalline materials, which can significantly increase this distance [33].

In order to investigate further the cause of reduced transition temperatures in the vicinity of the edges, high-resolution

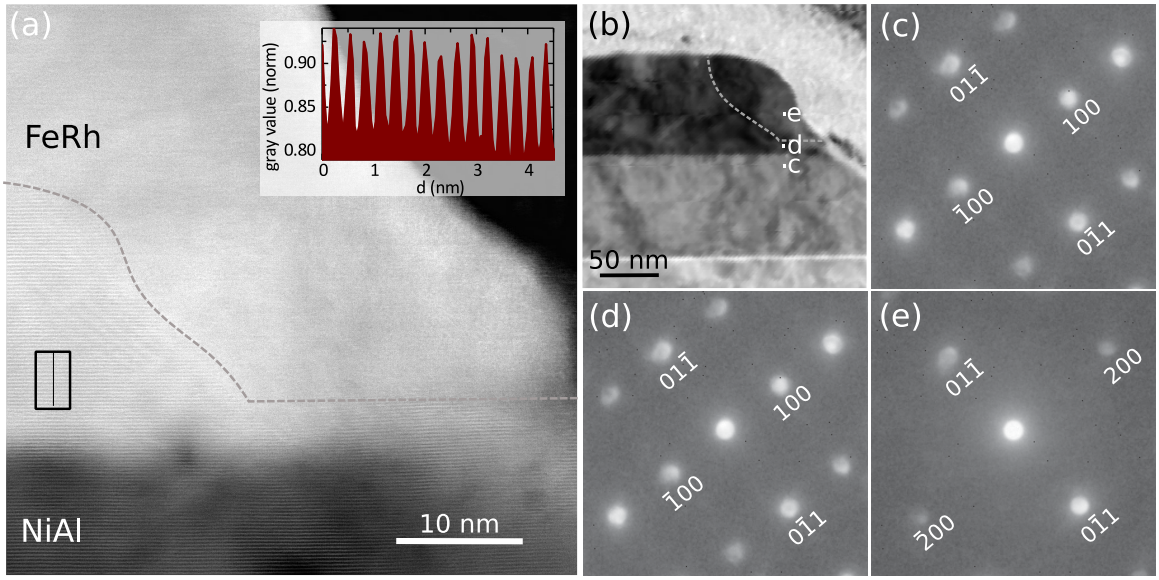

FIG. 8. STEM analysis of the patterned island edge. (a) High-resolution STEM image of the right-hand edge of the 5-μm island shown in Fig. 1(d). Inset: Vertical line scan over the indicated region showing lattice fringes; these fringes are not observed in the edge grain region above and to the right of the dashed gray line. (b) Bright-field image with diffraction contrast over a larger region and dashed gray line showing continuation of grain. (c)–(e) Nanodiffraction images of points indicated in (b).

STEM imaging was performed. A high-resolution STEM image of the edge region is shown in Fig. 8(a). Contrast in the image is dominated by the atomic number and hence the FeRh layer exhibits a higher average intensity than the NiAl buffer layer. In a region towards the left-hand side of the FeRh layer, greater than ∼30 nm away from the island edge, and throughout the NiAl layer, horizontally oriented lattice fringes are observed. In the FeRh layer the periodicity of these fringes is 0.294 ± 0.004 nm, consistent with the FeRh lattice parameter, and thus relates to the ⟨001⟩ lattice planes. Such fringes are only allowed to be visible where the B2, chemically ordered crystal structure exists (they are forbidden for chemically disordered bcc). Hence, the complete presence of fringes in the NiAl layer but only in part of the FeRh located away from the edge is suggestive of patterning-induced structural modification.

The nature of the crystal structure modification in this region was further investigated using four-dimensional nanobeam diffraction imaging. The edge region was probed with a parallel (<1-mrad semiconvergence angle), nanofocused electron beam (6-nm diameter). Scanning the beam, diffraction patterns were recorded using a high-speed electron counting detector [34] at each point in a 256×256 raster. Figures 8(b)–8(e) show this analysis, highlighting the image (essentially a bright-field image showing diffraction contrast) and diffraction patterns from the regions where lattice fringes were observed in the NiAl and FeRh and from the edge region where fringes were absent in Fig. 8(a).

In Figs. 8(c) and 8(d) the diffraction patterns from the FeRh and NiAl are identical in form and consistent with diffraction from the B2 structure when viewed along the [011] direction. In the region nearest the edge [Fig. 8(e)], the diffraction pattern contains significantly fewer spots and is consistent with a chemically disordered bcc crystal structure in this region. Relating this observation to the island edge contrast apparent in Fig. 8(b) [and also more weakly in the HAADF image shown in Fig. 1(d)], it can be seen that the structural modification extends over a larger region, composing a "grain" which extends in approximately 100 nm from the island edge and up to the top surface of the FeRh, taking an approximately 4% volume ratio of the island. Similar image contrast was observed at the opposite edge of the island (not shown).

While this chemically disordered modified crystal structure region is smaller than the approximately 250-nm edge domain nucleation region seen in the PEEM images, it is likely to be the cause of the lowered transition temperature due the high sensitivity of the transition on the alloy chemical order and structure [30]. The mismatch between the size of the observed edge grain and the nucleated domains may simply be a consequence of where the cross section was taken, the disordered grain may vary in width along the length of the island as the magnetic domains do.

IV. CONCLUSION

The mixed phase domains in FeRh have been imaged during transition and have shown three distinct modes of development—nucleation, growth, and merging—each proceeding at a higher energy cost than the last. The cost of the latter mode is attributed to the magnetostatic energy of ferromagnetic domain formation. Mixed phase domains have been studied in confined FeRh structures with sizes above and below the phase domain length scale. For 5- and 1-μm islands the edge and central regions were separated with a 14 K reduction in the transition temperature on the edges.

The cause of this reduction in transition temperature is a chemically disordered region within 100 nm of the island edge observed in cross-sectional high-resolution STEM. This is thought to arise from collision damage during low-energy ion milling. For the 0.5-μm structure the transition temperature was lowered a further 10 K due to the reduced number of merging events in the smaller space. In general, as patterning is used to produce features of ever smaller size, particular care will need to be taken over inevitable sidewall damage in subtractive patterning, to which FeRh is particularly sensitive. Strain relief is inevitable but its effects would be reduced in thinner films.

Data associated with this work are available from the Research Data Leeds repository under a CC-BY license [35]. The dataset supporting Figs. 8(a)–8(e) has been made available [36].

ACKNOWLEDGMENTS

We thank Diamond Light Source for beam time and we are grateful to M. C. Rosamond for assistance in the nanofabrication process and G. Stefanou for work on the SEM imaging. This work was financially supported by the EPSRC under Grant Nos. EP/M018504/1 and EP/M019020/1.

[1] L. H. Lewis, C. H. Marrows, and S. Langridge, Coupled magnetic, structural, and electronic phase transitions in FeRh, J. Phys. D: Appl. Phys. **49**, 323002 (2016).

[2] S. Maat, J.-U. Thiele, and E. E. Fullerton, Temperature and field hysteresis of the antiferromagnetic-to-ferromagnetic phase transition in epitaxial FeRh films, Phys. Rev. B **72**, 214432 (2005).

[3] Z. Q. Liu, L. Li, Z. Gai, J. D. Clarkson, S. L. Hsu, A. T. Wong, L. S. Fan, M. W. Lin, C. M. Rouleau, T. Z. Ward, H. N. Lee, A. S. Sefat, H. M. Christen, and R. Ramesh, Full Electroresistance Modulation in a Mixed-Phase Metallic Alloy, Phys. Rev. Lett. **116**, 097203 (2016).

[4] R. O. Cherifi, V. Ivanovskaya, L. C. Phillips, A. Zobelli, I. C. Infante, E. Jacquet, V. Garcia, S. Fusil, P. R. Briddon, N. Guiblin, A. Mougin, A. A. Ünal, F. Kronast, S. Valencia, B. Dkhil, A. Barthélémy, and M. Bibes, Electric-field control of magnetic order above room temperature, Nat. Mater. **13**, 345 (2014).

[5] R. Barua, F. Jiménez-Villacorta, and L. H. Lewis, Predicting magnetostructural trends in FeRh-based ternary systems, Appl. Phys. Lett. **103**, 102407 (2013).

[6] I. Suzuki, T. Naito, M. Itoh, and T. Taniyama, Barkhausen-like antiferromagnetic to ferromagnetic phase transition driven by spin polarized current, Appl. Phys. Lett. **107**, 082408 (2015).

[7] J.-U. Thiele, S. Maat, and E. E. Fullerton, FeRh/FePt exchange spring films for thermally assisted magnetic recording media, Appl. Phys. Lett. **82**, 2859 (2003).

[8] X. Marti, I. Fina, C. Frontera, J. Liu, P. Wadley, Q. He, R. J. Paull, J. D. Clarkson, J. Kudrnovský, I. Turek, J. Kuneš, D. Yi, J.-H. Chu, C. T. Nelson, L. You, E. Arenholz, S. Salahuddin, J. Fontcuberta, T. Jungwirth, and R. Ramesh, Room-temperature antiferromagnetic memory resistor, Nat. Mater. **13**, 367 (2014).

[9] T. Moriyama, N. Matsuzaki, K. J. Kim, I. Suzuki, T. Taniyama, and T. Ono, Sequential write-read operations in FeRh antiferromagnetic memory, Appl. Phys. Lett. **107**, 122403 (2015).

[10] C. Baldasseroni, C. Bordel, A. X. Gray, A. M. Kaiser, F. Kronast, J. Herrero-Albillos, C. M. Schneider, C. S. Fadley, and F. Hellman, Temperature-driven nucleation of ferromagnetic domains in FeRh thin films, Appl. Phys. Lett. **100**, 262401 (2012).

[11] C. J. Kinane, M. Loving, M. A. de Vries, R. Fan, T. R. Charlton, J. S. Claydon, D. A. Arena, F. Maccherozzi, S. S. Dhesi, D. Heiman, C. H. Marrows, L. H. Lewis, and S. Langridge, Observation of a temperature dependent asymmetry in the domain structure of a Pd-doped FeRh epilayer, New J. Phys. **16**, 113073 (2014).

[12] C. Baldasseroni, C. Bordel, C. Antonakos, A. Scholl, K. H. Stone, J. B. Kortright, and F. Hellman, Temperature-driven growth of antiferromagnetic domains in thin-film FeRh, J. Phys.: Condens. Matter **27**, 256001 (2015).

[13] T. P. Almeida, R. Temple, J. Massey, K. Fallon, D. McGrouther, T. Moore, C. H. Marrows, and S. McVitie, Quantitative TEM imaging of the magnetostructural and phase transitions in FeRh thin film systems, Sci. Rep. **7**, 17835 (2017).

[14] C. Le Graët, T. R. Charlton, M. McLaren, M. Loving, S. A. Morley, C. J. Kinane, R. M. D. Brydson, L. H. Lewis, S. Langridge, and C. H. Marrows, Temperature controlled motion of an antiferromagnet-ferromagnet interface within a dopant-graded FeRh epilayer, APL Mater. **3**, 041802 (2015).

[15] A. Ceballos, Z. Chen, O. Schneider, C. Bordel, L. W. Wang, and F. Hellman, Effect of strain and thickness on the transition temperature of epitaxial FeRh thin-films, Appl. Phys. Lett. **111**, 172401 (2017).

[16] C. Gatel, B. Warot-Fonrose, N. Biziere, L. A. Rodríguez, D. Reyes, R. Cours, M. Castiella, and M. J. Casanove, Inhomogeneous spatial distribution of the magnetic transition in an iron-rhodium thin film, Nat. Commun. **8**, 15703 (2017).

[17] F. Pressacco, V. Uhlíř, M. Gatti, A. Bendounan, E. E. Fullerton, and F. Sirotti, Stable room-temperature ferromagnetic phase at the FeRh(100) surface, Sci. Rep. **6**, 22383 (2016).

[18] C. W. Barton, T. A. Ostler, D. Huskisson, C. J. Kinane, S. J. Haigh, G. Hrkac, and T. Thomson, Substrate induced strain field in FeRh epilayers grown on single crystal MgO (001) substrates, Sci. Rep. **7**, 44397 (2017).

[19] V. Uhlíř, J. A. Arregi, and E. E. Fullerton, Colossal magnetic phase transition asymmetry in mesoscale FeRh stripes, Nat. Commun. **7**, 13113 (2016).

[20] J. A. Arregi, M. Horký, K. Fabianová, R. Tolley, E. E. Fullerton, and V. Uhlíř, Magnetization reversal and confinement effects across the metamagnetic phase transition in mesoscale FeRh structures, J. Phys. D: Appl. Phys. **51**, 105001 (2018).

[21] C. Le Graët, M. A. de Vries, M. McLaren *et al.*, Sputter growth and characterization of metamagnetic B2-ordered FeRh epilayers, J. Vis. Exp. **80**, e50603 (2013).

[22] C. Baldasseroni, G. K. Pálsson, C. Bordel, S. Valencia, A. A. Unal, F. Kronast, S. Nemsak, C. S. Fadley, J. A. Borchers, B. B. Maranville, and F. Hellman, Effect of capping material on interfacial ferromagnetism in FeRh thin films, J. Appl. Phys. **115**, 043919 (2014).

[23] M. A. de Vries, M. Loving, A. P. Mihai, L. H. Lewis, D. Heiman, and C. H. Marrows, Hall-effect characterization of the metamagnetic transition in FeRh, New J. Phys. **15**, 013008 (2013).

[24] J. W. Kim, P. J. Ryan, Y. Ding, L. H. Lewis, M. Ali, C. J. Kinane, B. J. Hickey, C. H. Marrows, and D. A. Arena, Surface influenced magnetostructural transition in FeRh films, Appl. Phys. Lett. **95**, 222515 (2009).

[25] R. Fan, C. J. Kinane, T. R. Charlton, R. Dorner, M. Ali, M. A. de Vries, R. M. D. Brydson, C. H. Marrows, B. J. Hickey, D. A. Arena, B. K. Tanner, G. Nisbet, and S. Langridge, Ferromagnetism at the interfaces of antiferromagnetic FeRh epilayers, Phys. Rev. B **82**, 184418 (2010).

[26] S. O. Mariager, L. Le Guyader, M. Buzzi, G. Ingold, and C. Quitmann, Imaging the antiferromagnetic to ferromagnetic first order phase transition of FeRh, arXiv:1301.4164.

[27] M. S. Cohen, Anomalous magnetic films, J. Appl. Phys. **33**, 2968 (1962).

[28] C. Himcinschi, R. Singh, I. Radu, A. P. Milenin, W. Erfurth, M. Reiche, U. Gösele, S. H. Christiansen, F. Muster, and M. Petzold, Strain relaxation in nanopatterned strained silicon round pillars, Appl. Phys. Lett. **90**, 021902 (2007).

[29] J. M. Shaw, S. E. Russek, T. Thomson, M. J. Donahue, B. D. Terris, O. Hellwig, E. Dobisz, and M. L. Schneider, Reversal mechanisms in perpendicularly magnetized nanostructures, Phys. Rev. B **78**, 024414 (2008).

[30] S. Cervera, M. Trassinelli, M. Marangolo, C. Carrétéro, V. Garcia, S. Hidki, E. Jacquet, E. Lamour, A. Lévy, S. Macé, C. Prigent, J. Rozet, S. Steydli, and D. Vernhet, Modulating the phase transition temperature of giant magnetocaloric thin films by ion irradiation, Phys. Rev. Materials **1**, 065402 (2017).

[31] M. J. McLaren, Transmission electron microscope characterisation of iron-rhodium epilayers, Ph.D. thesis, University of Leeds, 2014.

[32] J. F. Zeigler, SRIM and TRIM, http://www.srim.org/

[33] D. Dobrev, Ion-beam induced texture formation in vacuum condensed thin metal films, Thin Solid Films **92**, 41 (1982).

[34] Merlin for EM; http://quantumdetectors.com/merlin-for-em/

[35] R. C. Temple, T. P. Almeida, J. R. Massey, K. Fallon, R. Lamb, S. A. Morley, F. Maccherozzi, S. S. Dhesi, D. McGrouther, S. McVitie, T. A. Moore, and C. H. Marrows, Data for "Antiferromagnetic-ferromagnetic phase domain development in nanopatterned FeRh islands," https://doi.org/10.5518/453 (2018).

[36] R. C. Temple, T. Almeida, J. R. Massey, K. Fallon, R. Lamb, D. McGrouther, S. McVitie, T. A. Moore, and C. H. Marrows, Data for Fig. 8 in "Antiferromagnetic-ferromagnetic phase domain development in nanopatterned FeRh islands," https://dx.doi.org/10.5525/gla.researchdata.683 (2018).

Correction: A second data availability statement and source listing have been added. The first data availability source was incomplete and has been fixed.